7-1-2021

Friedel oscillations in graphene gapped by breaking $\mathcal{P}$ and T symmetries: Topological and geometrical signatures of electronic structure

Jin Yang

Ding-Fu Shao

Shu-Hui Zhang

Wen Yang

Friedel oscillations in graphene gapped by breaking $\mathcal{P}$ and $\mathcal{T}$ symmetries: Topological and geometrical signatures of electronic structure

Jin Yang,[1,2] Ding-Fu Shao [ORCID],[3] Shu-Hui Zhang [ORCID],[1,*] and Wen Yang [ORCID][2,†]

[1]*College of Mathematics and Physics, Beijing University of Chemical Technology, Beijing 100029, China*
[2]*Beijing Computational Science Research Center, Beijing 100193, China*
[3]*Department of Physics and Astronomy and Nebraska Center for Materials and Nanoscience, University of Nebraska–Lincoln, Lincoln, Nebraska 68588-0299, USA*

The measurement of Friedel oscillations (FOs) is conventionally used to recover the energy dispersion of electronic structure. Besides the energy dispersion, the modern electronic structure also embodies other key ingredients such as the geometrical and topological properties; it is one promising direction to explore the potential of FOs for the relevant measurement. Here, we present a comprehensive study of FOs in substrate-supported graphene under off-resonant circularly polarized light, in which a valley-contrasting feature and topological phase transition occur due to the combined breaking of inversion ($\mathcal{P}$) and time reversal ($\mathcal{T}$) symmetries. Depending on the position of the Fermi level, FOs may be contributed by electronic backscattering in one single valley or two valleys. In the single-valley regime, the oscillation periods of FOs can be used to determine the topological phase boundary of electronic structure, while the amplitudes of FOs distinguish trivial insulators and topological insulators in a quantitative way. In the two-valley regime, the unequal Fermi surfaces lead to a beating pattern (robust two-wave-front dislocations) of FOs contributed by intravalley (intervalley) scattering. This study implies the great potential of FOs in characterizing topological and geometrical properties of the electronic structure of two-dimensional materials.

I. INTRODUCTION

Friedel oscillations (FOs) represent the basic interference phenomenon of electronic waves when they are scattered by unintentional or intentional imperfection in crystalline materials [1]. FOs are determined by the electronic backscattering on the Fermi surface, then are used as a conventional tool to reconstruct the energy dispersion of the electronic structure by performing the energy-resolved scanning tunneling microscopy (STM) measurement [2,3]. Besides the energy dispersion, the geometrical and topological properties further enrich the modern electronic structure; their possible measurement by FOs has become one promising topic.

Graphene has been studied for nearly two decades since its seminal discovery [4]. However, the unique lattice and electronic structure make graphene the model system for the exploration of various interesting phenomena [5]. Among these phenomena, FOs have attracted wide theoretical [6–18] and experimental [19–23] interest since one can intentionally introduce a single-atom vacancy on sublattice site A or B in the present experimental conditions [23]. In particular, by counting the wave-front dislocations of FOs, two recent experiments [24,25] realized the measurement of the geometrical nature of the wave functions, namely, the Berry phase [26]. It underlies a lot of exotic phenomena such as Klein tunneling

[27,28] and the index shift of the quantum Hall effect in graphene [29–31] and is regarded as another key ingredient of the electronic structure [32,33]. The successful measurement of the geometrical Berry phase [24,25] without applying the magnetic field as usual [28–30,32] encourages us to explore the potential of FOs to identify the topology of the electronic structure.

Graphene can be made topological by using external methods; the key is the gap opening, which also dictates a lot of novel physics [34,35] and potential applications [36]. The usual ways to open the gap of graphene can be classified into two mechanisms, i.e., inversion symmetry ($\mathcal{P}$) breaking and time reversal symmetry ($\mathcal{T}$) breaking. In experiments and devices, graphene is usually placed on a specific substrate, i.e., substrate-supported graphene, in which proximity coupling effectively breaks $\mathcal{P}$ of graphene and then induces gap opening [37]. The Floquet engineering, namely, the control of the electronic structure using periodic driving, provides the other popular $\mathcal{T}$-breaking mechanism for gap opening [38], e.g., illuminating graphene by using off-resonant circularly polarized light [39]. The substrate-supported graphene under off-resonant circularly polarized light hosts a valley-contrasting feature and topological phase transition even without spin-orbit coupling [40], which provides an ideal platform to study the potential of FOs to characterize the topological and geometrical properties of the electronic structure.

One recent experiment [41] probed the band topology of a one-dimensional photonic insulator through the wave-front dislocations of FOs using the celebrated Su-Schrieffer-Heeger

———————
*shuhuizhang@mail.buct.edu.cn
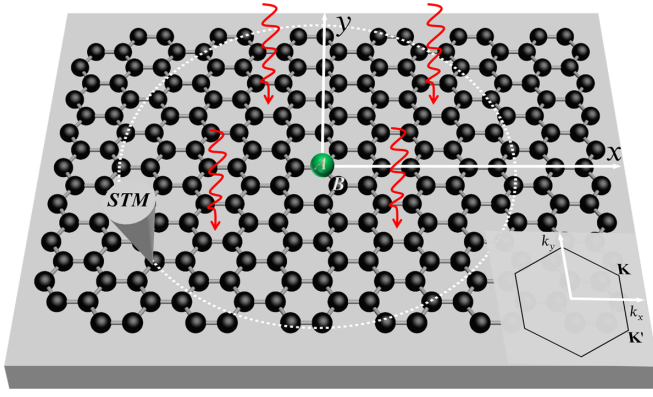†wenyang@csrc.ac.cn

035402-1

FIG. 1. Schematic measurement of vacancy-induced electronic Friedel oscillations by STM in substrate-supported graphene under off-resonant circularly polarized light. The honeycomb lattice of graphene with two inequivalent sublattice A and B is colored black, while the substrate is gray. The vacancy is represented by the green dot at the origin of the coordinate system. The substrate-supported graphene is radiated by the light from above (the red wavy lines). And the Brillouin zone in reciprocal space is shown in the inset, in which there are two inequivalent valleys, $\mathbf{K}$ and $\mathbf{K}'$.

model [42] as one example. In this study, we study FOs in substrate-supported graphene under off-resonant circularly polarized light. Depending on the position of the Fermi level, FOs may be contributed by the electronic scattering in one single valley or two valleys. In the single-valley regime, the oscillation periods of FOs trace the evolution of the electronic structure and then signify the topological phase boundary, while the amplitudes of FOs straightforwardly distinguish trivial insulators and topological insulators in a quantitative way without resorting to the edge states as in angle-resolved photoemission spectroscopy [43] and transport measurement [44]. In the two-valley regime, the unequal Fermi surfaces lead to the beating pattern of FOs contributed by intravalley scattering, and the robust two-wave-front dislocations of FOs are contributed by the intervalley scattering due to the energy-independent pseudospin texture. Therefore, beyond the conventional ability of FOs to recover energy dispersion,, this study shows the great potential of FOs in identifying the topological and geometrical properties of the electronic structure in two-dimensional materials.

The rest of this study is organized as follows. In Sec. II, we introduce the model structure and the T-matrix approach to describe the electronic scattering by one intentional vacancy. In Sec. III, we present our numerical calculations to show the unique features of the FOs in the single-valley and two-valley regimes and identify the signatures of the topological and geometrical properties of electronic structure by using the analytical formulas. Finally, we briefly summarize this study in Sec. IV.

II. THEORETICAL FORMALISM

Figure 1 illustrates the schematic model structure in this study; it shows the substrate-supported graphene under off-resonant circularly polarized light and can be described by the effective Hamiltonian (see the Appendix)

$$H_\xi = v_F(\xi \sigma_x k_x - \sigma_y k_y) + (\Delta - \xi F)\sigma_z \quad (1)$$

by using the sublattice basis of $\{A, B\}$, where $\xi = \pm$ represents two inequivalent valleys, $\mathbf{K}$ and $\mathbf{K}'$, in graphene, e.g., $\mathbf{K} = (\frac{2\pi}{3}, \frac{2\pi}{3\sqrt{3}})$ and $\mathbf{K}' = (\frac{2\pi}{3}, -\frac{2\pi}{3\sqrt{3}})$, as shown in the inset of Fig. 1, and $\sigma_{x,y,z}$ is the Pauli matrix acting on the pseudospin space. H_ξ includes two gap terms induced by the $\mathcal{P}$-breaking and $\mathcal{T}$-breaking mechanisms, $\Delta \sigma_z$ and $\xi F \sigma_z$ (see the Appendix for its derivation), which are very different in the sense of their independence and dependence on the valley index ξ. In addition, v_F is the Fermi velocity of graphene [45]. The energy dispersion and the spinor wave function are, respectively,

$$E_\lambda(\mathbf{k}) = \lambda v_F \sqrt{\kappa_\xi^2 + k^2} \quad (2)$$

and

$$\psi_{\lambda,\mathbf{k}} = \frac{1}{\sqrt{1 + k^2/(q_\lambda + \kappa_\xi)^2}} \begin{bmatrix} 1 \\ \frac{\xi k_x - i k_y}{q_\lambda + \kappa_\xi} \end{bmatrix}. \quad (3)$$

For convenience, we define the reduced quantities $\kappa_\xi = (\Delta - \xi F)/v_F$ and $q_\lambda = E_\lambda/v_F$, with $\lambda = \pm 1$, for the conduction and valence bands. Due to the combined effect of gap opening induced by breaking $\mathcal{P}$ and $\mathcal{T}$, graphene can realize the valley-contrasting feature and topological phase transition even without the spin-orbit coupling [40]. The valley-contrasting and topological physics will bring new features to FOs induced by the intentional introduction of a single-atom vacancy on an arbitrary sublattice site of graphene [23], e.g., on sublattice A, as shown by the green dot in Fig. 1. And the physics is essentially the same for the other vacancy configuration [46]. One can use STM to measure the corresponding change in the space-resolved and energy-resolved local density of states (LDOS) [17,47]:

$$\delta\rho(\mathbf{R}, \varepsilon) = -\frac{1}{\pi} \mathrm{Im}\left[\mathrm{Tr}\, \delta\mathbf{G}(\mathbf{R}, \mathbf{R}, \varepsilon)\right], \quad (4)$$

where

$$\delta\mathbf{G} = \mathbf{G} - \mathbf{G}^0 = \mathbf{G}^0(\mathbf{R}_2, \mathbf{0}, \varepsilon)\mathbf{T}(\varepsilon)\mathbf{G}^0(\mathbf{0}, \mathbf{R}_1, \varepsilon) \quad (5)$$

represents the change in the total Green's function (GF) $\mathbf{G}$ incorporating the effect of the vacancy relevant to the unperturbed GF $\mathbf{G}^0$ of the host system. Due to the translation invariance of the host system, the position arguments of $\mathbf{G}^0$ can be abbreviated by $\mathbf{R} = \mathbf{R}_2 - \mathbf{R}_1$ as used below. Equations (4) and (5) together show a clear physical meaning; that is, the STM tip at $\mathbf{R}$ emits the electron wave, as shown by the GF $\mathbf{G}^0(\mathbf{0}, \mathbf{R}, \varepsilon)$, leading to scattering by the vacancy at $\mathbf{0}$ back to the STM tip, as shown by the GF $\mathbf{G}^0(\mathbf{R}, \mathbf{0}, \varepsilon)$. Here, we use the T-matrix approach to describe the effect of a vacancy whose potential is simulated by $V_0\delta(\mathbf{r})$. The accurate value of V_0 is irrelevant to our physical results, and we use $V_0 = 3$ eV in the specific numerical calculations. And the T matrix is [17]

$$\mathbf{T}(\varepsilon) = \mathbf{V}\left[\mathbf{I} - \int d^2\mathbf{k}\, \mathcal{G}^0(\mathbf{k}, \varepsilon)\mathbf{V}\right]^{-1}. \quad (6)$$

In the T-matrix approach, $\mathbf{V}$ is usually a matrix, and its form depends on the specific position of the vacancy. For Fig. 1 and

using the sublattice basis of $\{A, B\}$, $\mathbf{V}$ has the form

$$\mathbf{V} = \begin{bmatrix} V_0 & 0 \\ 0 & 0 \end{bmatrix}. \tag{7}$$

Then, the T-matrix has the explicit expression

$$\mathbf{T}(\varepsilon) = \begin{bmatrix} t(\varepsilon) & 0 \\ 0 & 0 \end{bmatrix}, \tag{8}$$

where $t(\varepsilon) = V_0/[1 - V_0 G_{AA}^0(0, \varepsilon)]$ is the only nonvanishing matrix element of the T matrix. Turning to the GF, for the

Hamiltonian H_ξ, the valley-contrasting GF in the momentum space is defined as $\mathcal{G}_\xi^0(\mathbf{k}, \varepsilon) \equiv (z - H_\xi)^{-1}$ and has the form

$$\mathcal{G}_\xi^0(\mathbf{k}, \varepsilon) = \frac{1}{z^2 - v_F^2(k^2 + \kappa_\xi^2)} \begin{bmatrix} \varepsilon_{+,\xi} & \xi v_F k e^{i\xi\theta_k} \\ \xi v_F k e^{-i\xi\theta_k} & \varepsilon_{-,\xi} \end{bmatrix}. \tag{9}$$

Here, $z = \varepsilon + i0^+$, with 0^+ for the retarded properties of the GF, and $\varepsilon_{\pm,\xi} = v_F(q \pm \kappa_\xi) = v_F q_{\pm,\xi}$, with $q = \varepsilon/v_F$. As a result, one can obtain the GF in real space, $\mathbf{G}^0(\mathbf{R}, \varepsilon) = \sum_{\xi=\pm} e^{i\mathbf{R}\cdot\mathbf{K}_\xi}/(2v_F)^2 \mathbf{G}_\xi^0(\mathbf{R}, \varepsilon)$, in which $\mathbf{G}_\xi^0(\mathbf{R}, \varepsilon)$ is given by the Fourier transform of $\mathcal{G}_\xi^0(\mathbf{k}, \varepsilon)$,

$$\mathbf{G}_\xi^0(\mathbf{R}, \varepsilon) = \begin{bmatrix} -i\varepsilon_{+,\xi}\mathcal{H}_0(u_\xi) & \xi\sqrt{\varepsilon_{+,\xi}\varepsilon_{-,\xi}}\mathcal{H}_1(u_\xi)e^{i\xi\theta_R} \\ \xi\sqrt{\varepsilon_{+,\xi}\varepsilon_{-,\xi}}\mathcal{H}_1(u_\xi)e^{-i\xi\theta_R} & -i\varepsilon_{-,\xi}\mathcal{H}_0(u_\xi) \end{bmatrix}. \tag{10}$$

Here, $u_\xi = R\sqrt{q_{+,\xi}q_{-,\xi}}$, where R (θ_R) is the module (azimuthal angle) of $\mathbf{R}$. And $\mathcal{H}_\nu$ is the Hankel function of the first kind in the order ν. As a result, for the intravalley scattering, the sublattice-resolved LDOSs are

$$\delta\rho_A^{\text{intra}}(\mathbf{R}, \varepsilon) = C_0 \, \text{Im}\left[t(\varepsilon) \sum_{\xi=\pm} q_{+,\xi}^2 \mathcal{H}_0^2(u_\xi)\right] \tag{11a}$$

$$\approx \frac{2C_0}{\pi R} \, \text{Im}\left[t(\varepsilon) \sum_{\xi=\pm} q_{+,\xi}\sqrt{\frac{q_{+,\xi}}{q_{-,\xi}}} e^{i(2u_\xi - \frac{\pi}{2})}\right], \tag{11b}$$

$$\delta\rho_B^{\text{intra}}(\mathbf{R}, \varepsilon) = C_0 \, \text{Im}\left[t(\varepsilon) \sum_{\xi=\pm} q_{+,\xi}q_{-,\xi} \mathcal{H}_1^2(u_\xi)\right] \tag{11c}$$

$$\approx \frac{2C_0}{\pi R} \, \text{Im}\left[t(\varepsilon) \sum_{\xi=\pm} \sqrt{q_{+,\xi}q_{-,\xi}} e^{i(2u_\xi + \frac{\pi}{2})}\right], \tag{11d}$$

and for the intervalley scattering, the sublattice-resolved LDOSs are

$$\delta\rho_A^{\text{inter}}(\mathbf{R}, \varepsilon) = 2C_0 \, \text{Im}\left[t(\varepsilon) \prod_{\xi=\pm} q_{+,\xi} \mathcal{H}_0(u_\xi)\right] \cos(\theta_A) \tag{12a}$$

$$\approx \frac{4C_0}{\pi R} \, \text{Im}\left[t(\varepsilon) \prod_{\xi=\pm} q_{+,\xi}^{3/4} q_{-,\xi}^{-1/4} e^{i(u_\xi - \frac{1}{4}\pi)}\right] \cos(\theta_A), \tag{12b}$$

$$\delta\rho_B^{\text{inter}}(\mathbf{R}, \varepsilon) = -2C_0 \, \text{Im}\left[t(\varepsilon) \prod_{\xi=\pm} \sqrt{q_{+,\xi}q_{-,\xi}} \mathcal{H}_1(u_\xi)\right] \cos(\theta_B) \tag{12c}$$

$$\approx -\frac{4C_0}{\pi R} \, \text{Im}\left[t(\varepsilon) \prod_{\xi=\pm} (q_{+,\xi}q_{-,\xi})^{\frac{1}{4}} e^{i(u_\xi + \frac{1}{4}\pi)}\right] \cos(\theta_B), \tag{12d}$$

where $C_0 = 1/(16\pi v_F^2)$, $\theta_A = \delta\mathbf{K}\cdot\mathbf{R}$, and $\theta_B = \delta\mathbf{K}\cdot\mathbf{R} - \delta\xi\theta_R$, with $\delta\mathbf{K} = \mathbf{K} - \mathbf{K}'$ and $\delta\xi = \xi - \xi'$. To obtain the approximate formulas in the long range, we have used the asymptotic expression for the Hankel function [48], $\mathcal{H}_\nu(u) \approx \sqrt{2}/\sqrt{\pi u} e^{i(u - \frac{\pi}{2}\nu - \frac{\pi}{4})}$.

III. RESULTS AND DISCUSSION

In this section, we present the numerical calculations to show the typical features of FOs in substrate-supported graphene under off-resonant circularly polarized light. The light (substrate) can break the $\mathcal{T}$ ($\mathcal{P}$) of graphene and induces the gap $2F$ (2Δ). By fixing $\Delta = 0.1$ eV and tuning

F, Figs. 2(a)–2(c) show the evolutive electronic structure of graphene in the presence of two kinds of gap openings. The combined effect of $2F$ and 2Δ gives rise to the valley-contrasting feature inherited from the $\mathcal{T}$-breaking gap. For the $\mathbf{K}$ valley (blue), its gap first closes and then reopens; for example, the values are 0.2, 0, and 0.2 eV in Figs. 2(a)–2(c), which implies the transition from a normal insulator to a topological insulator [40]. But the gap in the $\mathbf{K}'$ valley (red) increases monotonously; for example, the values are 0.2, 0.4, and 0.6 eV in Figs. 2(a)–2(c). Due to the valley-contrasting electronic structure, the Fermi surface also displays the evolution behaviors with changing the position of the Fermi level. (i) One can obtain two different regimes, single-valley and two-valley
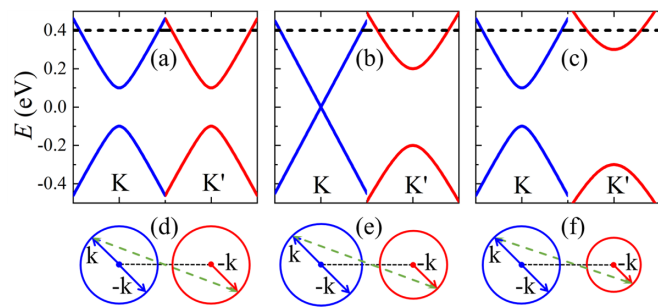
FIG. 2. Evolutive electronic structure of graphene gapped by breaking time reversal and inversion symmetries, $2F$ and 2Δ, respectively. With $\Delta = 0.1$ eV, $F = 0$, 0.1, and 0.2 eV in (a), (b), and (c), respectively. The combining effect of $2F$ and 2Δ leads to the valley-contrasting feature; the gap of the **K** valley (blue) first closes and then reopens, implying the occurrence of a topological transition [40], while that of the **K′** valley (red) increases monotonously. Thus, (a) and (c) represent, respectively, the normal insulator and the (valley-polarized) topological insulator, although the gap values of their **K** valleys are equal, and (b) is gapless at the phase boundary. (d)–(f) are the corresponding Fermi surfaces of (a)–(c) when the same Fermi level (dashed line) is tuned to arrive at the two-valley regime in each case. The valley-contrasting Fermi surfaces are equal in (d), and they are unequal in (e) and (f). In the two-valley regime, Friedel oscillations are contributed by the intravalley and intervalley backscattering, as shown in (d)–(f).

ones. Figures 2(a)–2(c) are in the two-valley regime since the same Fermi level is higher than the gap values of the two valleys. Two Fermi surfaces are shown clearly in Figs. 2(d)–2(f) for Figs. 2(a)–2(c). (ii) The Fermi surface contours of the two valleys are unequal for graphene with nonzero F and Δ, e.g., in Figs. 2(e) and 2(f), which is very different from the case in Fig. 2(d). FOs reflect the intrinsic Fermi surface property, which should reveal the electronic structure of graphene gapped by broken $\mathcal{T}$ and $\mathcal{P}$ and exhibit the unique features. In addition, FOs are dominated by the backscattering events of electrons upon the imperfection, which can be divided into intravalley scattering and intervalley scattering, as shown in Figs. 2(d)–2(f). In the following, we present the unique features of intravalley scattering and intervalley scattering to FOs in single-valley and two-valley regimes and briefly discuss the experimental feasibility to observe them.

A. Single-valley regime

When the Fermi level is tuned to lower than the $\mathcal{P}$-breaking gap, i.e., $\varepsilon < \Delta$, the single-valley regime arises. Figure 3 shows the evolutive electronic structure of graphene in the single-valley regime ($\varepsilon = 0.09$ eV and $\Delta = 0.1$ eV) and the corresponding FOs with changing the $\mathcal{T}$-breaking gap F. Here, the right-circularly polarized light is considered (see the Appendix); then the topological transition occurs in the **K** valley ($\xi = +$). Corresponding to different cases in Fig. 3(a), Figs. 3(b) and 3(c) show the FOs contributed by the intravalley scattering on sublattices A and B, $\delta\rho_A^{\text{intra}}$ and $\delta\rho_B^{\text{intra}}$, respectively. $\delta\rho_A^{\text{intra}}$ and $\delta\rho_B^{\text{intra}}$ are calculated exactly (blue) and approximately (red) in Figs. 3(b) and 3(c), and the good consistence at long range can be seen. The features are similar to those in doped gapless graphene [7,14–16,49]. On the one

hand, FOs exhibit the dimension-determined decay $1/R$ which can be inferred from the analytical equations (11b) and (11d); then they are multiplied by R to account for this intrinsic decay. On the other hand, the oscillations of $\delta\rho_A^{\text{intra}}$ and $\delta\rho_B^{\text{intra}}$ have a phase difference π, which can also be obtained by comparing Eqs. (11b) and (11d) in the single-valley regime. And the oscillation periods are determined by half Fermi wavelengths, $\pi R/u_+ = \pi/\sqrt{q^2 - \kappa_+^2}$. So the oscillation periods are tunable by the $\mathcal{T}$-breaking gap F.

Most importantly, FOs can reflect the topological property of the electronic structure. (i) There is a critical value that is the shortest oscillation period signifying the gapless **K** valley, which is actually at the topological phase boundary. As a result, FOs can be used to track the topological boundary since it can be measured easily by STM. (ii) The amplitude of the sublattice-resolved LDOS in the normal phase can be far larger than those in the topological phase; for example, considering the identical gap value, $\delta\rho_A^{\text{intra}}(\mathbf{R}, \varepsilon) \propto q_{\pm, \xi}^{3/2} q_{\mp, \xi}^{-1/2}$, in the normal (topological) phase, the amplitude difference is up to one order of magnitude in Fig. 3(b). Therefore, FOs can be used to distinguish the trivial insulator and the topological insulator in a quantitative way and do not resort to the edge states of topological insulators as in other experimental techniques, e.g., the visual observation of edge states by angle-resolved photoemission spectroscopy [43] and the quantized conductance plateau contributed by the edge state in the transport measurement [44]. Note that the amplitudes of $\delta\rho_B^{\text{intra}}$ ($\delta\rho_A^{\text{intra}}$) in different insulator phases have no quantitative difference when the vacancy is on sublattice A (B).

B. Two-valley regime

When the Fermi level is tuned to higher than the sum of the $\mathcal{T}$-breaking and $\mathcal{P}$-breaking gaps, i.e., $\varepsilon > \Delta + F$, the two-valley regime arises. As a result, the intravalley and intervalley scattering events together contribute to FOs, which are both revealed by unique features, i.e., the beating pattern and wavefront dislocations, respectively.

1. Beating pattern

Figure 4 shows $\delta\rho_A^{\text{intra}}$ and $\delta\rho_B^{\text{intra}}$ contributed by intravalley scattering in the two-valley regime. $\delta\rho_A^{\text{intra}}$ ($\delta\rho_B^{\text{intra}}$) is shown in the left (right) column. To fix $\Delta = 0.1$ eV and $\varepsilon = 0.3$ eV, we consider two values of F, i.e., 0.08 and 0.12 eV in the top and bottom rows, respectively. Due to unequal Fermi surfaces of the two valleys, there are two basic oscillation periods, which are $\pi R/u_+ = \pi/\sqrt{q^2 - \kappa_+^2}$ and $\pi R/u_- = \pi/\sqrt{q^2 - \kappa_-^2}$ from Eqs. (11b) and (11d). More interesting, the beating pattern occurs, and its period is $\pi R/(u_+ - u_-) = \pi(\sqrt{q^2 - \kappa_+^2} - \sqrt{q^2 - \kappa_-^2})^{-1}$, as shown in Fig. 4. Previously, the beating pattern in FOs was shown in the two-dimensional electron gas [50], graphene [51], the MoS_2 monolayer [52], and silicene [53], which all require spin-orbit coupling. In our case, the effect of spin-orbit coupling is realized by the $\mathcal{T}$-breaking light field. The beating pattern reflects the unequal Fermi surfaces and was suggested to characterize the topological transition of silicene in a previous study [53]; the relevant discussion
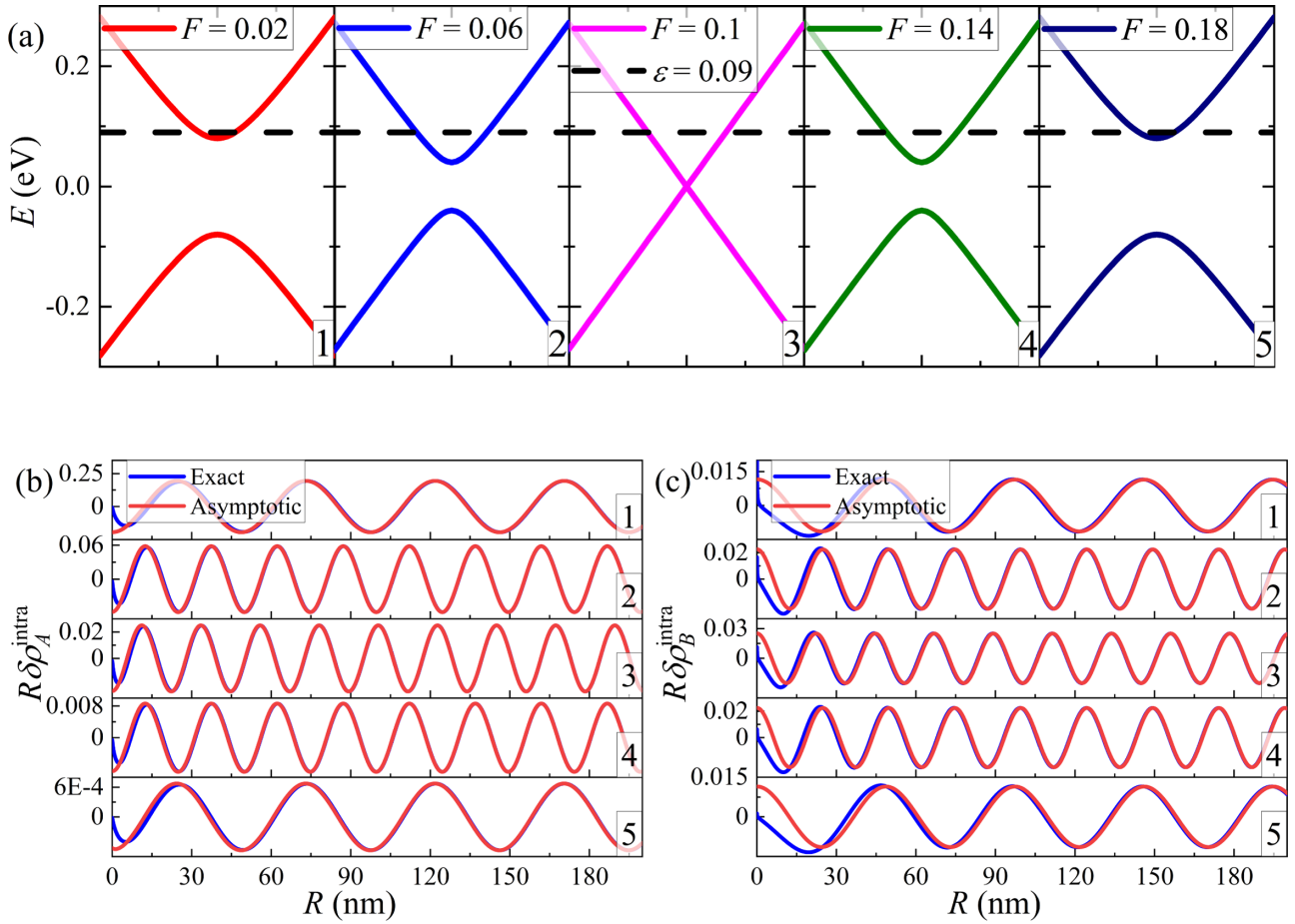
FIG. 3. Evolutive electronic structure of graphene in the single-valley regime and the corresponding Friedel oscillations. (a) is the electronic structures of valley **K** with changing F when the Fermi level is $\varepsilon = 0.09$ eV and $\Delta = 0.1$ eV. Corresponding to different cases in (a), (b) and (c) show the Friedel oscillations $\delta\rho_A^{\text{intra}}$ and $\delta\rho_B^{\text{intra}}$ contributed by intravalley scattering on sublattices A and B, respectively. $\delta\rho_{A,B}^{\text{intra}}$ is calculated exactly (blue) and approximately (red) and is multiplied by R to account for the intrinsic $1/R$ decay.

there is also applicable to our case. The $\mathcal{T}$-breaking field in our case and spin-orbit coupling in silicene [53] give rise
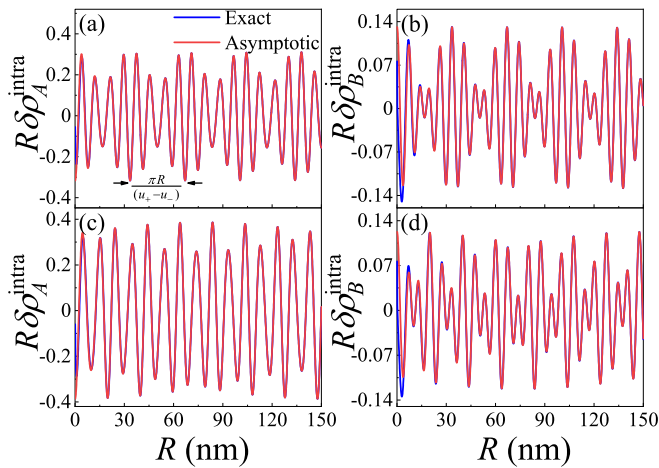

FIG. 4. Beating pattern of Friedel oscillations $\delta\rho_A^{\text{intra}}$ and $\delta\rho_B^{\text{intra}}$ contributed by intravalley scattering in the two-valley regime. $\delta\rho_A^{\text{intra}}$ ($\delta\rho_B^{\text{intra}}$) is shown in the left (right) column. $F = 0.08$ eV (0.12 eV) in the top (bottom) row. Here, $\Delta = 0.1$ eV, and $\varepsilon = 0.3$ eV.

to the same novel phenomena, i.e., the topological transition and beating pattern; their comparability and interplay deserve further study, e.g., in silicene under off-resonant circularly polarized light.

2. Wave-front dislocations

The oscillation periods of FOs are inversely proportional to the momentum changes in the backscattering events. Compared to the contribution from intervalley scattering, the intravalley scattering contribution to FOs has a rather longer period and is thus more remarkable. As a result, the intravalley scattering contribution to FOs has been well studied by a lot of theoretical [6–18] and experimental [19–23] efforts.

Recently, the importance of the intervalley scattering was highlighted [24,25,46,54] because the corresponding FOs may show the wave-front dislocations, which are the fingerprints of geometrical quantities, e.g., the Berry phase in gapless graphene [24,25] and the winding number in gapped graphene [46]. In a previous work [46], the $\mathcal{P}$-breaking gap was considered, and there was no valley-contrasting feature, and the Fermi surfaces of the two valleys were equal. By further incorporating the $\mathcal{T}$-breaking gap, the intervalley scattering occurs between the unequal Fermi surfaces, as shown
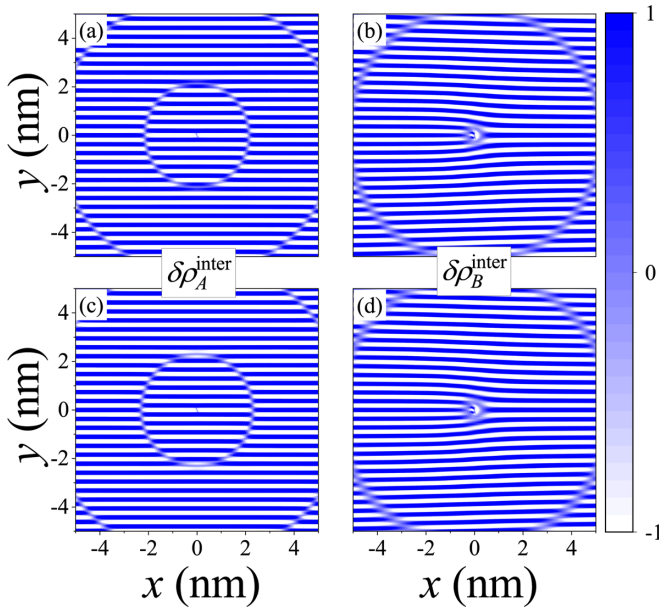
FIG. 5. Wave-front dislocations of Friedel oscillations $\delta\rho_A^{\text{inter}}$ and $\delta\rho_B^{\text{inter}}$ contributed by intervalley scattering in the two-valley regime. $\delta\rho_A^{\text{inter}}$ ($\delta\rho_B^{\text{inter}}$) is shown in the left (right) column. $F = 0.08$ eV (0.12 eV) in the top (bottom) row. Here, $\Delta = 0.1$ eV, and $\varepsilon = 0.3$ eV.

in Figs. 2(e) and 2(f). Figure 5 shows $\delta\rho_A^{\text{inter}}$ and $\delta\rho_B^{\text{inter}}$ contributed by the intervalley scattering in the two-valley regime. $\delta\rho_A^{\text{inter}}$ ($\delta\rho_B^{\text{inter}}$) is shown in the left (right) column, and their amplitudes are multiplied by R to avoid the intrinsic decay $1/R$ based on the analytical equations (12b) and (12d). By adopting $F = 0.08$ eV (0.12 eV) in the top (bottom) row, one can see the normal oscillating wave fronts perpendicular to $\delta\mathbf{K}$ with a wavelength $\lambda_{\delta\mathbf{K}} = 2\pi/|\delta\mathbf{K}| \approx 0.37$ nm in $\delta\rho_A^{\text{inter}}(\mathbf{R}, \varepsilon)$ and two wave-front dislocations at $\mathbf{R} = 0$ accommodating the phase accumulated along a contour enclosing the singular point of the phase θ_R [55] in $\delta\rho_B^{\text{inter}}(\mathbf{R}, \varepsilon)$. These features are identical to those in graphene with a single $\mathcal{P}$-breaking gap Δ in the previous work [46], which demonstrates the robustness of wave-front dislocations against the gap opening explained by the invariant winding number of the pseudospin vector. The pseudospin vector can be defined as $\mathbf{s} = \langle\psi_{\lambda,\mathbf{k}}|(\sigma_x, \sigma_y)|\psi_{\lambda,\mathbf{k}}\rangle = (s_x, s_y)$, with

$$s_x = \frac{2\xi k_x(q_\lambda + \kappa_\xi)}{(q_\lambda + \kappa_\xi)^2 + k^2} = \frac{\xi k_x}{q_\lambda}, \tag{13a}$$

$$s_y = -\frac{2k_y(q_\lambda + \kappa_\xi)}{(q_\lambda + \kappa_\xi)^2 + k^2} = -\frac{k_y}{q_\lambda}. \tag{13b}$$

Obviously, the pseudospin texture, which is determined by the azimuthal angle of $\mathbf{s}$, is invariant on different Fermi surfaces. Therefore, this study further demonstrates the robustness of wave-front dislocations of FOs in graphene against the $\mathcal{T}$-breaking light field, which causes the unequal Fermi surfaces for the intervalley scattering. In light of the topological origin of wave-front dislocations (i.e., originating from the topological winding number [46]), one can recall the edge states of the topological insulator, but the edge states of topological insulators are susceptible to $\mathcal{T}$-breaking perturbation [56]. These different responses, i.e., robustness

(susceptibility), of wave-front dislocations (edge states) to $\mathcal{T}$-breaking external field (perturbation) should reflect their bulk and edge nature.

3. Experimental feasibility

Here, we briefly discuss the possible observation of the topological and geometrical properties of the electronic structure by using FOs. First, we consider a realistic model structure, i.e., substrate-supported graphene under off-resonant circularly polarized light, as shown by Fig. 1. The key is the magnitude of the gap opening induced by the $\mathcal{P}$-breaking and $\mathcal{T}$-breaking mechanisms. On the one hand, when the proper substrate is chosen, e.g., graphene epitaxially grown on a silicon dioxide substrate, the $\mathcal{P}$-breaking gap ranges from several to hundreds of meV [57,58]. So it is proper to adopt $\Delta = 0.1$ eV in our numerical calculations. In addition, the substrate with a high dielectric constant for two-dimensional graphene, effectively reducing the electron-electron interaction [59], which is significant in the one-dimensional system [60], is a better choice for experiments. On the other hand, the $\mathcal{T}$-breaking gap F is manipulated by the amplitude (or intensity) and frequency of the off-resonant light (see the Appendix), which can be up to the same magnitude as the $\mathcal{P}$-breaking one, as discussed in Ref. [40], e.g., $F = 0.1$ eV induced by the experimental available soft x-ray regime with frequency 3500 THz and intensity 10^{13} W/cm^2. In particular, the light-induced anomalous Hall effect was observed in graphene [61], which indicated the giant experimental advance of transport measurement under intense light. Second, the Fermi level in Fig. 1 can be adjusted through a global back gate [45]; then the single-valley regime and two-valley regime can be addressed handily. To avoid the trigonal warping effect of the Fermi surface, the Fermi level should not go beyond the linear dispersion region of graphene, i.e., less than 1 eV relative to the Dirac point [45]. Third, in ballistic graphene, the residual weak disorders are up to several nanometers or more away from each other, so they have a trivial effect on the FOs induced by a single vacancy [54]. FOs have been used to measure the geometrical Berry phase by using STM [24,25]. Our work is the direct theoretical extension of these two experiments [24,25], so future verification is very feasible.

IV. CONCLUSIONS

In this study, we studied Friedel oscillations of electrons in substrate-supported graphene under off-resonant circularly polarized light, in which there are a valley-contrasting feature and topological phase transition induced by the combined breaking of $\mathcal{P}$ and $\mathcal{T}$ symmetries. By tuning the position of the Fermi level, two regimes arise, i.e., the single-valley regime and the two-valley regime, in which FOs are contributed by the electronic backscattering in one single valley and two valleys, respectively. In the single-valley regime, FOs can reflect the topological property of the electronic structure. A critical oscillation period corresponds to the topological phase boundary, and their amplitudes can be used to distinguish a trivial insulator and a topological insulator in a quantitative way without resorting to edge states as in angle-resolved

photoemission spectroscopy or transport measurements. In the two-valley regime, the Fermi surfaces of two valleys are unequal, which leads to the beating pattern for the intravalley scattering and the robust two-wave-front dislocations due to the energy-independent pseudospin texture for the intervalley scattering. This study used graphene as an example to show the great potential of FOs to identify the topological and geometrical properties of the electronic structure of two-dimensional materials, which expands the ability of FOs as a conventional tool to recover energy dispersion.

APPENDIX: THE DERIVATION OF THE EFFECTIVE HAMILTONIAN

In this Appendix, we present the derivation of the Hamiltonian of substrate-supported graphene under intense off-resonant circularly polarized light [40], i.e., Eq. (1) in the main text. The intrinsic Hamiltonian of substrate-supported graphene is

$$H_0 = v_F(\xi\sigma_x k_x - \sigma_y k_y) + \Delta\sigma_z, \qquad (A1)$$

where Δ depends on the breaking degree of $\mathcal{P}$ of graphene by the substrate. For the electrons in graphene, the off-resonant circularly polarized light of the frequency ω introduces the time-dependent vector potential, which is

$$\mathbf{A}(t) = A_0[-\eta\sin(\omega t)\mathbf{e}_x + \cos(\omega t)\mathbf{e}_y]. \qquad (A2)$$

Here, $\eta = \mp$ denotes the right (left) circularly polarized light. Including the vector potential, we have to make the replacement $k_x \to k_x - \eta e A_0 \sin(\omega t)$ and $k_y \to k_y + e A_0 \cos(\omega t)$ in the Hamiltonian H_0. Under the condition $e A v_F \ll \omega$, the electron-photon scattering is limited to two low-order processes, i.e., the emission and the absorption of a single virtual photon and its conjugate process; one can express the effective time-independent Hamiltonian as

$$H_\xi \approx H_0 + \frac{[H_{-1}, H_1]}{\omega}, \qquad (A3)$$

where

$$H_m = \frac{1}{T}\int_0^T dt\, e^{im\omega} H_0, \qquad (A4)$$

with $T = 2\pi/\omega$ being the period of light. $H_{\pm 1} = \frac{1}{2}e A v_F(\pm\eta\sigma_x + \xi\sigma_y)$ leads to $[H_{-1}, H_1] = -\eta\xi e^2 A^2 v_F^2 \sigma_z$. As a result, the effective Floquet Hamiltonian is

$$H_\xi = \hbar v_F(\xi\sigma_x k_x - \sigma_y k_y) + (\Delta - \xi F_\eta)\sigma_z, \qquad (A5)$$

where $F_\eta = \eta(e A v_F)^2/\omega$. The right or left circularly polarized light leads to the same physics, so $\eta = -1$ is used and not explicitly shown in Eq. (1) in the main text.

[1] J. Friedel, London, Edinburgh Dublin Philos. Mag. J. Sci. **43**, 153 (1952).

[2] L. Simon, C. Bena, F. Vonau, M. Cranney, and D. Aubel, J. Phys. D **44**, 464010 (2011).

[3] L. Chen, P. Cheng, and K. Wu, J. Phys.: Condens. Matter **29**, 103001 (2017).

[4] K. S. Novoselov, A. K. Geim, S. V. Morozov, D. Jiang, Y. Zhang, S. V. Dubonos, I. V. Grigorieva, and A. A. Firsov, Science **306**, 666 (2004).

[5] X. Feng, J. Zhu, W. Wu, and S. A. Yang, arXiv:2103.13772.

[6] V. V. Cheianov and V. I. Fal'ko, Phys. Rev. Lett. **97**, 226801 (2006).

[7] C. Bena, Phys. Rev. Lett. **100**, 076601 (2008).

[8] E. H. Hwang and S. Das Sarma, Phys. Rev. Lett. **101**, 156802 (2008).

[9] T. Pereg-Barnea and A. H. MacDonald, Phys. Rev. B **78**, 014201 (2008).

[10] C. Bena, Phys. Rev. B **79**, 125427 (2009).

[11] F. M. D. Pellegrino, G. G. N. Angilella, and R. Pucci, Phys. Rev. B **80**, 094203 (2009).

[12] A. Bácsi and A. Virosztek, Phys. Rev. B **82**, 193405 (2010).

[13] G. Gómez-Santos and T. Stauber, Phys. Rev. Lett. **106**, 045504 (2011).

[14] J. A. Lawlor, S. R. Power, and M. S. Ferreira, Phys. Rev. B **88**, 205416 (2013).

[15] M. Settnes, S. R. Power, D. H. Petersen, and A.-P. Jauho, Phys. Rev. B **90**, 035440 (2014).

[16] M. Settnes, S. R. Power, J. Lin, D. H. Petersen, and A.-P. Jauho, Phys. Rev. B **91**, 125408 (2015).

[17] C. Dutreix and M. I. Katsnelson, Phys. Rev. B **93**, 035413 (2016).

[18] T. M. Rusin and W. Zawadzki, Phys. Rev. B **97**, 205410 (2018).

[19] G. M. Rutter, J. N. Crain, N. P. Guisinger, T. Li, P. N. First, and J. A. Stroscio, Science **317**, 219 (2007).

[20] I. Brihuega, P. Mallet, C. Bena, S. Bose, C. Michaelis, L. Vitali, F. Varchon, L. Magaud, K. Kern, and J. Y. Veuillen, Phys. Rev. Lett. **101**, 206802 (2008).

[21] P. Mallet, I. Brihuega, S. Bose, M. M. Ugeda, J. M. Gómez-Rodríguez, K. Kern, and J. Y. Veuillen, Phys. Rev. B **86**, 045444 (2012).

[22] K. W. Clark, X.-G. Zhang, G. Gu, J. Park, G. He, R. M. Feenstra, and A.-P. Li, Phys. Rev. X **4**, 011021 (2014).

[23] H. González-Herrero, J. M. Gömez-Rodríguez, P. Mallet, M. Moaied, J. J. Palacios, C. Salgado, M. M. Ugeda, J.-Y. Veuillen, F. Yndurain, and I. Brihuega, Science **352**, 437 (2016).

[24] C. Dutreix, H. Gonzalez-Herrero, I. Brihuega, M. I. Katsnelson, C. Chapelier, and V. T. Renard, Nature (London) **574**, 219 (2019).

[25] Y. Zhang, Y. Su, and L. He, Phys. Rev. Lett. **125**, 116804 (2020).

[26] M. V. Berry, Proc. R. Soc. London, Ser. A **392**, 45 (1984).

[27] M. I. Katsnelson, K. S. Novoselov, and A. K. Geim, Nat. Phys. **2**, 620 (2006).

[28] A. F. Young and P. Kim, Nat. Phys. **5**, 222 (2009).

[29] K. S. Novoselov, A. K. Geim, S. V. Morozov, D. Jiang, M. I. Katsnelson, I. V. Grigorieva, S. V. Dubonos, and A. A. Firsov, Nature (London) **438**, 197 (2005).

[30] Y. Zhang, Y.-W. Tan, H. L. Stormer, and P. Kim, Nature (London) **438**, 201 (2005).

[31] K. S. Novoselov, E. McCann, S. V. Morozov, V. I. Falko, M. I. Katsnelson, U. Zeitler, D. Jiang, F. Schedin, and A. K. Geim, Nat. Phys. **2**, 177 (2006).

[32] D. Xiao, M.-C. Chang, and Q. Niu, Rev. Mod. Phys. **82**, 1959 (2010).

[33] D. Vanderbilt, *Berry Phases in Electronic Structure Theory: Electric Polarization, Orbital Magnetization and Topological Insulators* (Cambridge University Press, Cambridge, 2018).

[34] F. Guinea, M. I. Katsnelson, and A. K. Geim, Nat. Phys. **6**, 30 (2010).

[35] D. Xiao, W. Yao, and Q. Niu, Phys. Rev. Lett. **99**, 236809 (2007).

[36] F. Schwierz, Nat. Nanotechnol. **5**, 487 (2010).

[37] A. Chaves, J. G. Azadani, H. Alsalman, D. R. da Costa, R. Frisenda, A. J. Chaves, S. H. Song, Y. D. Kim, D. He, J. Zhou, A. Castellanos-Gomez, F. M. Peeters, Z. Liu, C. L. Hinkle, S.-H. Oh, P. D. Ye, S. J. Koester, Y. H. Lee, Ph. Avouris, X. Wang, and T. Low, npj 2D Mater. Appl. **4**, 29 (2020).

[38] T. Oka and S. Kitamura, Annu. Rev. Condens. Matter Phys. **10**, 387 (2019).

[39] J. Cayssol, B. Dóra, F. Simon, and R. Moessner, Phys. Status Solidi RRL **7**, 101 (2013).

[40] X. Zhai and G. Jin, Phys. Rev. B **89**, 235416 (2014).

[41] C. Dutreix, M. Bellec, P. Delplace, and F. Mortessagne, Nat. Commun. **12**, 3571 (2021).

[42] W. P. Su, J. R. Schrieffer, and A. J. Heeger, Phys. Rev. Lett. **42**, 1698 (1979).

[43] S. Tang, C. Zhang, D. Wong, Z. Pedramrazi, H.-Z. Tsai, C. Jia, B. Moritz, M. Claassen, H. Ryu, S. Kahn, J. Jiang, H. Yan, M. Hashimoto, D. Lu, R. G. Moore, C.-C. Hwang, C. Hwang, Z. Hussain, Y. Chen, M. M. Ugeda, Z. Liu, X. Xie, T. P. Devereaux, M. F. Crommie, S.-K. Mo, and Z.-X. Shen, Nat. Phys. **13**, 683 (2017).

[44] M. König, S. Wiedmann, C. Brüne, A. Roth, H. Buhmann, L. W. Molenkamp, X.-L. Qi, and S.-C. Zhang, Science **318**, 766 (2007).

[45] A. H. Castro Neto, F. Guinea, N. M. R. Peres, K. S. Novoselov, and A. K. Geim, Rev. Mod. Phys. **81**, 109 (2009).

[46] S.-H. Zhang, J. Yang, D.-F. Shao, Z. Wu, and W. Yang, Phys. Rev. B **103**, L161407 (2021).

[47] Y.-L. Zou, J. Song, C. Bai, and K. Chang, Phys. Rev. B **94**, 035431 (2016).

[48] M. Abramowitz and I. A. Stegun, *Handbook of Mathematical Functions with Formulas, Graphs, and Mathematical Table* (Dover, New York, 1970), p. 364.

[49] C. Bena, C. R. Phys. **17**, 302 (2016).

[50] S. M. Badalyan, A. Matos-Abiague, G. Vignale, and J. Fabian, Phys. Rev. B **81**, 205314 (2010).

[51] A. Scholz, T. Stauber, and J. Schliemann, Phys. Rev. B **86**, 195424 (2012).

[52] A. Scholz, T. Stauber, and J. Schliemann, Phys. Rev. B **88**, 035135 (2013).

[53] H.-R. Chang, J. Zhou, H. Zhang, and Y. Yao, Phys. Rev. B **89**, 201411(R) (2014).

[54] Y. Zhang, Y. Su, and L. He, Nano Lett. **21**, 2526 (2021).

[55] J. F. Nye, M. V. Berry, and F. C. Frank, Proc. R. Soc. London, Ser. A **336**, 165 (1974).

[56] X.-L. Qi and S.-C. Zhang, Rev. Mod. Phys. **83**, 1057 (2011).

[57] S. Y. Zhou, G.-H. Gweon, A. V. Fedorov, P. N. First, W. A. de Heer, D.-H. Lee, F. Guinea, A. H. Castro Neto, and A. Lanzara, Nat. Mater. **6**, 770 (2007).

[58] E. Rotenberg, A. Bostwick, T. Ohta, J. L. McChesney, T. Seyller, and K. Horn, Nat. Mater. **7**, 258 (2008).

[59] A. Konar, T. Fang, and D. Jena, Phys. Rev. B **82**, 115452 (2010).

[60] R. Egger and H. Grabert, Phys. Rev. Lett. **75**, 3505 (1995).

[61] J. W. McIver, B. Schulte, F.-U. Stein, T. Matsuyama, G. Jotzu, G. Meier, and A. Cavalleri, Nat. Phys. **16**, 38 (2020).